

Temporal evolution of arch filaments as seen in He I 10830 Å

S.J. González Manrique^{1,2,3}, C. Kuckein², M. Collados⁴, C. Denker², S.K. Solanki^{5,6}, P. Gömöry¹,
M. Verma², H. Balthasar², A. Lagg⁵, and A. Diercke^{2,3}

¹ Astronomical Institute, Slovak Academy of Sciences, 05960 Tatranská Lomnica, Slovak Republic

² Leibniz-Institut für Astrophysik Potsdam (AIP), An der Sternwarte 16, 14482 Potsdam, Germany

³ Institut für Physik and Astronomie, Universität Potsdam, Karl-Liebknecht-Straße 24/25, 14476 Potsdam-Golm, Germany

⁴ Instituto de Astrofísica de Canarias, c/ Vía Láctea s/n, 38205 La Laguna, Tenerife, Spain

⁵ Max-Planck-Institut für Sonnensystemforschung, Justus-von-Liebig-Weg 3, 37077 Göttingen, Germany

⁶ School of Space Research, Kyung Hee University, Yongin, Gyeonggi-Do, 446-701, Republic of Korea

e-mail: smanrique@ta3.sk

Received January 22, 2018; accepted June 18, 2018

ABSTRACT

Aims. We study the evolution of an arch filament system (AFS) and of its individual arch filaments to learn about the processes occurring in them.

Methods. We observed the AFS at the GREGOR solar telescope on Tenerife at high cadence with the very fast spectroscopic mode of the GREGOR Infrared Spectrograph (GRIS) in the He I 10830 Å spectral range. The He I triplet profiles were fitted with analytic functions to infer line-of-sight (LOS) velocities to follow plasma motions within the AFS.

Results. We tracked the temporal evolution of an individual arch filament over its entire lifetime, as seen in the He I 10830 Å triplet. The arch filament expanded in height and extended in length from 13'' to 21''. The lifetime of this arch filament is about 30 min. About 11 min after the arch filament is seen in He I, the loop top starts to rise with an average Doppler velocity of 6 km s⁻¹. Only two minutes later, plasma drains down with supersonic velocities towards the footpoints reaching a peak velocity of up to 40 km s⁻¹ in the chromosphere. The temporal evolution of He I 10830 Å profiles near the leading pore showed almost ubiquitous dual red components of the He I triplet, indicating strong downflows, along with material nearly at rest within the same resolution element during the whole observing time.

Conclusions. We followed the arch filament as it carried plasma during its rise from the photosphere to the corona. The material then drained toward the photosphere, reaching supersonic velocities, along the legs of the arch filament. Our observational results support theoretical AFS models and aids in improving future models.

Key words. Sun: chromosphere – Sun: activity – Methods: observational – Methods: data analysis – Techniques: high angular resolution

1. Introduction

An important role in solar physics in general, and in solar activity in particular, is played by the emergence of magnetic flux at the solar surface. The generally accepted theory states that emerging flux regions (EFRs) are formed by magnetic flux tubes that are transported to the solar surface by buoyancy (Parker 1955; Zwaan 1987; Caligari et al. 1995). The process forms Ω -loops and can lead to active regions. After the flux finishes rising to the photosphere, the active regions start to decay (van Driel-Gesztelyi & Green 2015).

An EFR as seen in the photosphere can evolve on many different temporal and spatial scales. The smallest EFRs have a lifetime of just a few minutes, while large active regions have a lifetime from days up to months (Archontis 2012).

Many different magnetic field elements emerge or disappear on the solar surface when EFRs form. In most cases, these elements evolve into bipolar structures. Smaller magnetic elements can appear and merge with the main bipole or are canceled with opposite polarity elements (Archontis 2012). In many EFRs the magnetic field between two opposite main polarities can form the well known “sea-serpent” topology (see, e.g., Harvey & Martin 1973; Pariat et al. 2004; Archontis 2012; Cheung & Isobe

2014; Schmieder et al. 2014). Emerging field lines can form a photospheric pattern of aligned dark intergranular lanes (Strous et al. 1996). In the chromosphere, EFRs become visible through magnetic loops loaded with plasma, which flows down towards both footpoints (Solanki et al. 2003). In this study, we observed a chromospheric arch filament system (AFS) connecting two photospheric pores (see Sect. 2).

The magnetic activity in the solar photosphere is characterized by various magnetic structures with a wide range of spatial sizes. The magnetic radius of pores is always larger than the continuum radius, which implies that a magnetic canopy exists (Keil et al. 1999; Buehler et al. 2015).

Velocities perpendicular to the surface and horizontal motions inside the concentrated magnetic fields of mature pores are generally close to zero for all photospheric heights, and the observed strong downflows in the surroundings range between 0.5 and 3 km s⁻¹ (see, e.g., Brants & Steenbeek 1985; Leka & Skumanich 1998; Hirzberger 2003; Sankarasubramanian & Rimmele 2003; Cho et al. 2010; Sobotka et al. 2012; Quintero Noda et al. 2016). Quintero Noda et al. (2016) measured small upward velocities up to 1 km s⁻¹ at mid-photospheric layers. Verma & Denker (2014) calculated the horizontal velocities of more than 2800 pores. Isolated pores exhibit minor inflows in

the interior and stronger outflows surrounding the pores, which reach up to 0.7 km s^{-1} .

The chromosphere above an EFR is best described as an AFS, which connects two regions of opposite magnetic polarity crossing the polarity inversion line. Bruzek (1967) reported these systems of fibrils for the first time and called them arch filament systems. The AFSs are prominently visible in line-core filtergrams of the strong chromospheric absorption line $H\alpha$ and also in the line core of the Ca II H & K lines (Bruzek 1969). More recently they were observed in the $\text{He I } 10830 \text{ \AA}$ triplet (e.g., Solanki et al. 2003; Spadaro et al. 2004; Lagg et al. 2004, 2007; Xu et al. 2010; Vargas Domínguez et al. 2012; Ma et al. 2015; González Manrique et al. 2016). Bruzek (1969) determined that the length of the arch filaments reaches the size of supergranular network cells (20–30 Mm). Typically, the width of individual AFS loops is only a few megameters, and the height of the arches varies between 5 and 15 Mm (Merenda et al. 2011) with a lifetime of about 30 min (Bruzek 1967). However, some individual loops of the AFS can reach heights close to 25 Mm and lengths of 20–40 Mm (Tsiropoula et al. 1992). Solanki et al. (2003) reported upflows in the center of the arches and downflows at the footpoints. Downflows reach velocities in the range of $30\text{--}50 \text{ km s}^{-1}$. They were observed near both footpoints of the AFS, whereas loop tops rise with about $1.5\text{--}20 \text{ km s}^{-1}$ (see, e.g., Bruzek 1969; Zwaan 1985; Chou & Zirin 1988; Lites et al. 1998; Solanki et al. 2003; Spadaro et al. 2004; González Manrique et al. 2017a).

A suitable spectral line to investigate chromospheric features and particularly AFSs is the He I at 10830 \AA triplet (Lagg et al. 2007; Xu et al. 2010). It forms in the upper chromosphere (Avrett et al. 1994) and consists of transitions between the upper levels $2^3P_{2,1,0}$ and the lower level 2^3S_1 . Two of the transitions overlap and consequently only two spectral lines can be observed. The nonblended line observed at 10829.09 \AA is commonly called the “blue” component and the blended line at 10830.30 \AA is called the “red” component. The exact wavelength positions were taken from the National Institute of Standards and Technology (NIST).¹

Several studies of the chromospheric dynamics have been carried out using the He I triplet. Particularly, very high downflow velocities were reported (e.g., Penn & Kuhn 1995; Muglach et al. 1997; Muglach & Sütterlin 1998). The observations very often show that two or more atmospheric components are present within the same spatial resolution element. It is possible that such complex, multicomponent profiles provide information of two or more different heights in the atmosphere. Schmidt et al. (2000) reported for the first time these “dual or multiple flows,” indicated by two or more peaks in the spectrum close to the He I triplet. In the case of only two components, it is common to find one of the peaks with subsonic velocities, called the “slow component,” while the other peak reaches supersonic velocities and is called the “fast component.” Flow speeds above 10 km s^{-1} in the He I triplet are considered to be supersonic (Aznar Cuadrado et al. 2005, 2007). Studies of AFS based on the He I triplet reported downflows of $15\text{--}90 \text{ km s}^{-1}$ (see, e.g., Solanki et al. 2003; Aznar Cuadrado et al. 2005, 2007; Sasso et al. 2007; Lagg et al. 2007; Balthasar et al. 2016; González Manrique et al. 2016). Results of the temporal evolution of dual-component $\text{He I } 10830 \text{ \AA}$ spectral profiles were presented in González Manrique et al. (2017b).

Solanki et al. (2003) investigated the magnetic field in an AFS, and reported magnetic field strengths in the footpoints be-

tween 390 and 500 G at chromospheric heights (as deduced from the He I triplet), the strength decreasing to 50 G at the tops of the arch filaments. Magnetic field strengths between 700 and 900 G were reported by Lagg et al. (2007) in regions with very high velocities, typically located at the footpoints. Xu et al. (2010) inferred the magnetic field strength showing an asymmetric distribution from the footpoint (800 G) to the loop tops (300 G). Solanki et al. (2003), and Xu et al. (2010) reconstructed the three-dimensional magnetic field in an AFS. They assumed that the $\text{He I } 10830 \text{ \AA}$ triplet is formed along the magnetic field loops, and Merenda et al. (2011) confirmed this assumption.

The new generation of solar telescopes and instruments allow us to record very high-resolution observations necessary to investigate the dynamics, magnetic field, and widths of arch filaments. These observations will help us to answer many open questions related to flux emergence (see the questions raised in the review by Cheung & Isobe 2014): (1) What are the observational consequences of the emerging flux (Bruzek 1967; Zwaan 1978)? (2) How do EFRs evolve with time in the different layers of the solar atmosphere and how are these layers linked? (3) Is it possible to measure the height difference between the photosphere and the chromosphere connected by the legs of the AFSs?

In Sect. 2 we present the observations. We describe image restoration and image processing in Sect. 3. In Sect. 4 we introduce the data analysis. In Sect. 5 we present the results, and analyze mainly the temporal evolution of the AFS using the unique observations of the very fast spectroscopic mode of GRIS (see Sect. 2) in the $\text{He I } 10830 \text{ \AA}$ spectral region. Finally, we discuss our findings and compare them with the more recent literature concerning the AFSs and EFRs in Sect. 6. Some initial results of this study were presented in González Manrique et al. (2016, 2017b).

2. Observations

An EFR smaller than a medium-sized active region, containing two principal pores with opposite polarities and an associated AFS in the chromosphere, was observed between 08:16 UT and 09:20 UT on 2015 April 17. The region of interest (ROI) is located at heliographic coordinates S19 and W4 ($\mu \equiv \cos \theta = 0.97$). The ground-based observations were performed with the GREGOR Infrared Spectrograph (GRIS, Collados et al. 2012) located at the 1.5-meter GREGOR solar telescope (Schmidt et al. 2012; Denker et al. 2012) at Observatorio del Teide, Tenerife, Spain. The overview of the EFR/AFS in Fig. 1 contains the field of view (FOV) of the high-resolution observations with GRIS, which is superposed on extreme ultraviolet (EUV) and continuum images and a photospheric magnetogram obtained with the Atmospheric Imaging Assembly (AIA, Lemen et al. 2012) and the Helioseismic and Magnetic Imager (HMI, Scherrer et al. 2012; Schou et al. 2012), respectively, both on board the Solar Dynamics Observatory (SDO, Pesnell et al. 2012) at 09:00 UT on 2015 April 17.

GRIS was operated in the very fast spectroscopic mode (no polarimetry) in the $\text{He I } 10830 \text{ \AA}$ spectral region (González Manrique et al. 2017b). With this fast mode, it is possible to scan the ROI at a much higher cadence with only a single exposure per slit position while accepting a higher noise level than in the standard polarimetric mode, which typically requires several accumulations for each polarization state. In addition, polarimetric information was purposefully discarded, again to achieve the high cadence required to investigate very dynamic processes in the chromosphere. Preliminary results obtained from this data set

¹ www.nist.gov

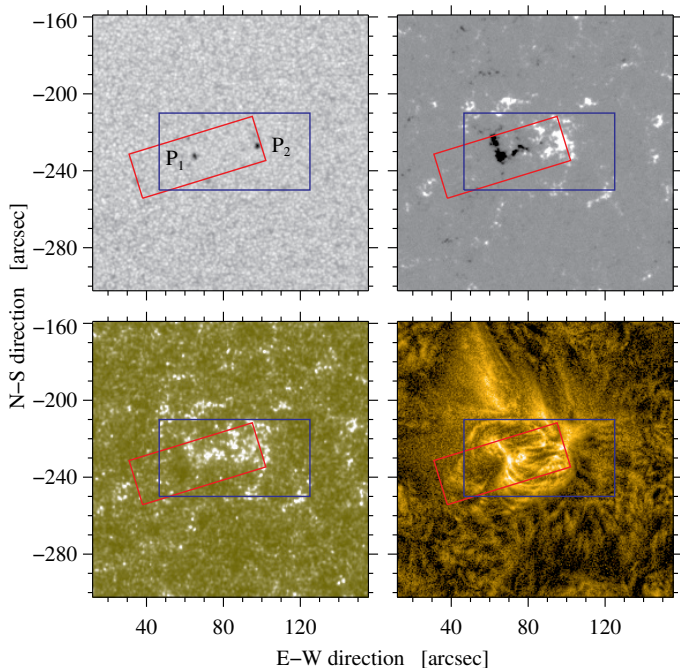


Fig. 1. Overview of the EFR at 09:00 UT on 2015 April 17: SDO HMI continuum image (*top left*), HMI magnetogram (*top right*), AIA 1600 Å image (*bottom left*), and NAFE-corrected AIA Fe IX 171 Å image (*bottom right*). The red rectangle delineates the FOV covered by GRIS. The blue rectangle represents the FOV where the temporal evolution of the magnetic flux was calculated (see Fig. 4).

discussing noise level and fitting procedures for dual-component He I 10830 Å spectral profiles were presented in González Manrique et al. (2016).

The observed spectral region covers a wavelength range in the near-infrared (NIR) of about 18 Å containing the photospheric Si I 10827 Å, Ca I 10834 Å, and Ca I 10839 Å lines; the chromospheric He I 10830 Å triplet; and other solar and telluric lines. The dispersion is $\delta_\lambda = 18.0 \text{ mÅ pixel}^{-1}$, and the number of spectral points along the wavelength axis is $N_\lambda = 1010$. The spatial step size and the pixel size along the slit are very similar, $0''.134$ and $0''.136$, respectively. The integration time is $t = 100 \text{ ms}$ for one accumulation. A spatial scan consists of 180 steps in total. Thus, the FOV is $66''.3 \times 24''.1$, and it takes about 58 s to cover it. This time interval includes overhead for reading out the camera and writing the data to disk. The observations continued for about one hour resulting in 64 spatio-spectral data cubes. The NIR spectra were taken under good seeing conditions. As shown in Fig. 2, the seeing changed during the time series, with extended periods of very good observing conditions. This is quantified by computing the rms-contrast of the granulation for each map. The values fluctuated between 1.5% and 2.9% for the continuum at $1.0 \mu\text{m}$ during the observing period. As a comparison, previous works found an rms-contrast at disk center of 6.1% and 2.9% for $0.8 \mu\text{m}$ and $1.5 \mu\text{m}$, respectively (Sánchez Cuberes et al. 2003). However, these values refer to imaging data with 2–4 times shorter exposure times. At around 09:00 UT the seeing conditions were good to very good with a granular rms-contrast between 2.2% and 2.9%. Therefore, the 45th scan at 09:00:56 UT (see Fig. 3) was selected as a reference for the GRIS data. The GREGOR Adaptive Optics System (GAOS, Berkefeld et al. 2012) provided real-time correction, ensuring a better quality of the spectral data cubes. GREGOR’s

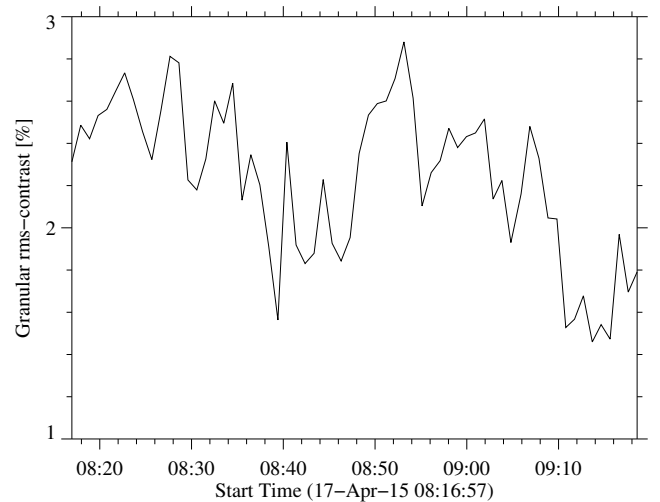


Fig. 2. Temporal evolution of the granular rms-contrast during the observing time with GRIS. In all figures the observing period refers to universal time.

alt-azimuthal mount (Volkmer et al. 2012) introduced an image rotation of 22.3° , which had to be corrected in the data reduction shrinking significantly the common FOV for the whole time series.

Context data are provided by SDO, where HMI takes full-disk filtergrams. The filtergrams are combined to form continuum intensity images, LOS magnetograms, and Dopplergrams at a 45 s cadence, and the image scale is $0''.5 \text{ pixel}^{-1}$. The longitudinal magnetograms are obtained with a precision of 10 G and allow us to track the temporal evolution of the magnetic flux contained within the active region. The response of upper atmospheric layers, i.e., the transition region and corona, is monitored at different plasma temperatures with EUV and UV images provided by AIA at a cadence of 12 s and 24 s, respectively. The image scale of $0''.6 \text{ pixel}^{-1}$ is slightly larger compared to HMI. The EUV images are beneficial for establishing the topology of low-lying filamentary structures and overarching loops, which are indicative of the magnetic connectivity within the active region and its surroundings.

3. Data reduction

Reduction and calibration of the GRIS data cube includes standard dark and flat-field corrections (González Manrique et al. 2016). Wavelength calibration comprises orbital motions and solar gravity redshift corrections, as described by Kuckein et al. (2012). Hence, the Doppler velocities refer to an absolute scale. Common fringes, dust particles along the slit, and abnormal intensity peaks are removed, and the proper continuum of the spectral line is determined. In addition, the telluric line at 10832.108 Å was eliminated from the spectra (González Manrique et al. 2016). This telluric line interferes in some cases with the fast component of the He I 10830 Å triplet. To remove the telluric line, every profile was normalized to the local continuum to ensure that the continuum of the telluric line conforms to $I_c = 1$. This normalization was only used to calculate the Doppler shifts explained in Sect. 4.2 and remove the telluric line. We computed a mean intensity profile for every map, assuming that the central wavelength of the telluric line is constant. We created a synthetic telluric profile by fitting the observed mean profile with a single Lorentzian profile. Subsequently, we divided every spectral pro-

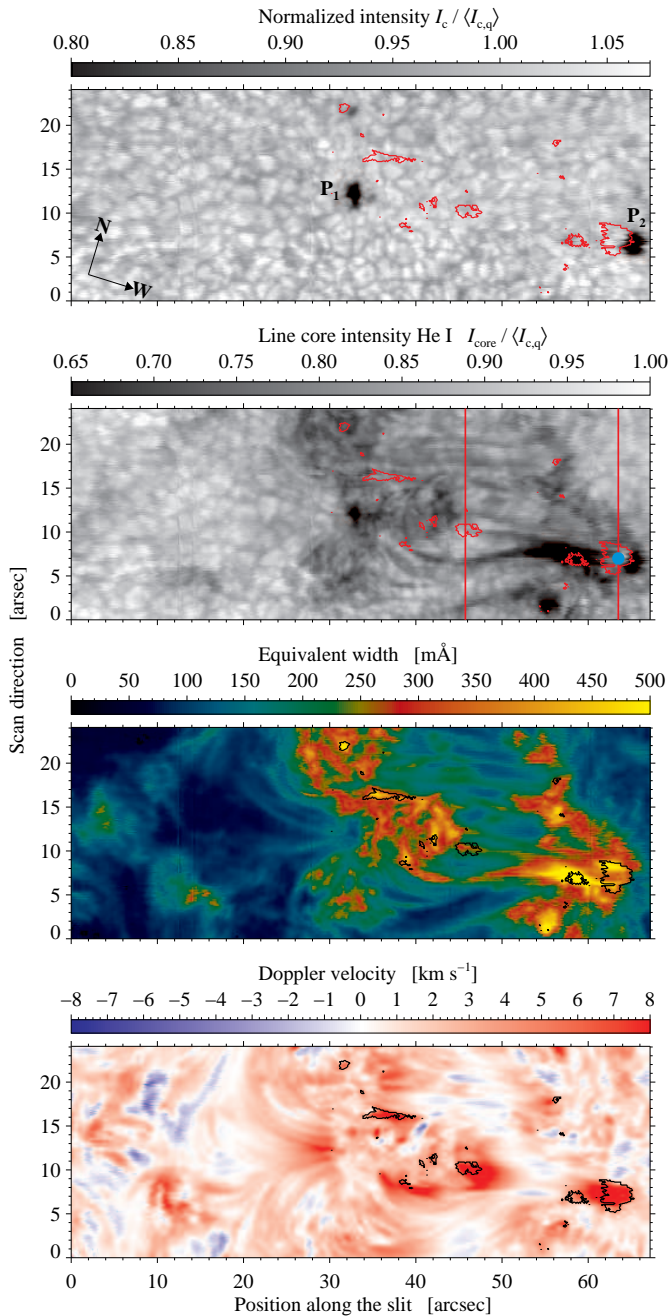


Fig. 3. Slit-reconstructed GRIS images at 09:00:56 UT on 2015 April 17 of the EFR centered on the pore P_1 with negative polarity shown in Fig. 1: continuum intensity, line core intensity of the red component of the He I triplet, equivalent width, and He I Doppler velocity calculated assuming only a single flow component (*top to bottom*). The blue filled circle (*second panel from top*) refers to the location of strong downflows near the pore P_2 , and it is used to calculate the average profiles in Fig. 6. The contours encompass dual-flow He I profiles. The red vertical lines indicate positions of the space-time diagrams (the right line corresponds to the upper panel of Fig. 10). The temporal evolution of the He I line depression and Doppler shifts is available as an online movie covering the period between 08:16:57 UT and 09:18:33 UT.

file of the map by the synthetic profile, effectively removing the telluric line. The slit-reconstructed continuum and the line-core intensity map of the red He I component are depicted in the first and second panel of Fig. 3, respectively.

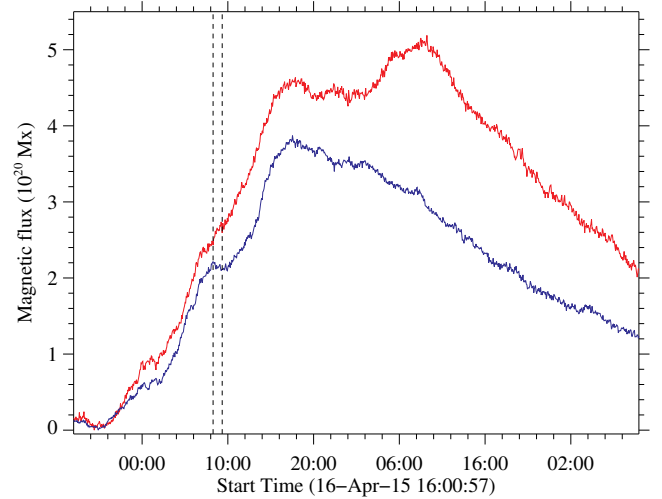


Fig. 4. Temporal evolution of new magnetic flux from HMI magnetograms covering the entire ROI (blue rectangle in Fig. 1). The red and blue solid lines represent the magnetic flux of the positive and negative polarity, respectively. The dashed vertical lines mark start and end of the high-resolution observations with GREGOR.

The AIA and HMI data were downloaded from the Virtual Solar Observatory (VSO) in level 1.0 and 1.5 format, respectively. The different AIA filtergrams and HMI data products are adjusted to a common coordinate system and image scale ($0''.6 \text{ pixel}^{-1}$). All data were compensated for differential rotation with respect to the central meridian. The reference image was taken at 00:00:57 UT on 2015 April 17 because at this time the EFR was exactly at the central meridian. The Fe IX 171 Å image in the bottom right panel of Fig. 1 is enhanced using the Noise Adaptive Fuzzy Equalization method (NAFE, Druckmüller 2013).

4. Data analysis

4.1. Temporal evolution of emerging magnetic flux

Our study of the temporal evolution of the emerging magnetic flux is based on time series of HMI magnetograms compensated for solar differential rotation. The considered HMI data cover both flux emergence and decay. The high-resolution GRIS data were recorded roughly in the middle of the flux emergence period (see vertical dashed lines in Fig. 4). To compute the magnetic flux, a blue rectangular ROI was selected encompassing the entire EFR (Fig. 3). The ROI extends in disk center coordinates from the bottom left corner ($+45'', -250''$) to the top right corner ($+125'', -210''$). The rise and decay of the magnetic flux is tracked for both magnetic polarities are shown in Fig. 4, where the red and blue curves correspond to the positive and negative magnetic polarities, respectively. The pre-existing magnetic flux was determined as the median value of a two-hour time series just before onset of the flux emergence at 16:00 UT on 2015 April 16 and was subtracted separately for each polarity; i.e., we only estimated the total amount of newly emerging flux.

4.2. Line-of-sight velocities of the He I 10830 Å triplet

Generally, the He I 10830 Å triplet in the observed data cube only consists of one blue and two blended red components. Nevertheless, a small percentage of spectral profiles reveals clear signatures of “dual flows” (Schmidt et al. 2000), which splits each

blue and red component into a slow and fast component (for a total of 4). The centroid of the slow component is commonly close to rest, while the centroid of the fast component is in most cases strongly redshifted. An approach to fit the two parts of the red component is described by González Manrique et al. (2016) based on a subset of the current data set. Initially, all profiles are fitted with a single Lorentzian profile using MPFIT (Markwardt 2009), a program written in the interactive data language (IDL). The wavelength range automatically adjusts to the line depths, i.e., it is broader for strong lines, to enhance the accuracy and stability of the fits. The slow component of the He I red component is potentially blended with the fast component of the He I blue component. The random and systematic errors induced by this method are small enough to allow scientific interpretation of the 2D maps of physical parameters. The wavelength reference for the LOS velocities is the average laboratory wavelength 10830.30 Å of the blended red component given by the NIST database.

In a second step, only dual-flow profiles are fitted with a double-Lorentzian profile. This deviates from the approach in González Manrique et al. (2016), where all profiles were fitted with a double-Lorentzian followed by an evaluation, whether single- or double-peaked profiles are more appropriate. In the current implementation dual-flow profiles are automatically detected based on the single-Lorentzian fits. Their locations are indicated by the red or black contours in all panels of Fig. 3. The selection criteria for dual-flow profiles are (1) a strong asymmetry between the blue and red line wings at half the line depth, (2) the presence of two clearly defined minima, (3) a large FWHM of the line profiles, and (4) a strongly redshifted line core with respect to the mean central wavelength.

5. Results

5.1. General description of the region of interest

The high-resolution observations cover a short period in the EFR lifetime, which is marked by dashed vertical lines in Fig. 4. At the time when the observations started, roughly half the final flux had already emerged (see Fig. 4). Thus, the outcome of this study primarily addresses questions related to ongoing flux emergence. The lifetime of the EFR, as observed with the SDO data (see Fig. 1), is about three days. The ROI has two main pores with opposite polarities. This bipolar region shows many properties of an active region, but likely does not carry enough flux to develop mature sunspots. The two pores become visible in HMI magnetograms at around 20:08 UT on 2015 April 16. In HMI continuum images, the pores appear around two hours later. Many small magnetic features with positive and negative polarities emerge between the two main pores. Some of them cancel each other, but others move until they merge with the main pore of the same polarity. The growth rate of the two polarities is roughly the same, with the exception of the observing time with GREGOR, where the negative polarity (blue) remains stationary over approximately two hours. The polarities during its lifetime were not balanced, i.e., the leading positive polarity (red) was dominant. This may reflect that the chosen ROI does not completely encompass the full bipolar region, that the flux moves across the boundary of the ROI, or that HMI is missing part of the flux (e.g., due to small inconsistencies in calibration of plage and pore fields).

Approximately one day after emergence, at 20:00 UT on 2015 April 17, the pores reached their maximum size and magnetic flux. While the negative polarity started to decay immedi-

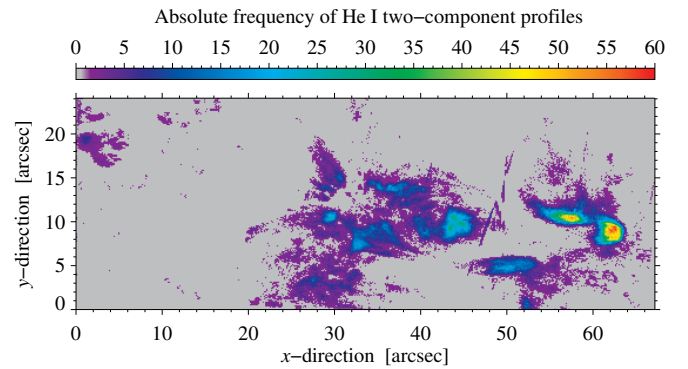


Fig. 5. Frequency of occurrence of dual-flow profiles during the observing period. The color bar represents the number of maps in which dual flows are present at a particular location.

ately, the positive polarity reached another maximum around 16 hours after the first one. The decay rate after the second maximum is clearly stronger for the positive polarity. The leading pore with positive polarity appears more fragmented, the negative pore is larger and has a diameter of around 5''. The negative flux reaches values up to 3.8×10^{20} Mx and the positive polarity up to 5×10^{20} Mx (see Fig. 4).

5.2. Description of the arch filament system

An AFS is visible in the chromosphere, as is seen in the line core intensity map of the red He I spectral line (Fig. 3). The qualitative differences between line core intensity and equivalent width (Fig. 3) are mainly produced by velocity broadening (or velocity induced splitting of the line profile into two components) and only to a very small degree by saturation (because the line is relatively weak). The arch filaments connect the two pores and other small-scale magnetic elements that are emerging mainly between them. The individual arch filaments change with time during the observations on timescales of minutes (see Sect. 5.4).

We investigated whether the observed AFS is visible in the corona, i.e., if the observed loop structures match those visible in AIA 304 Å He II maps. Even though the He I triplet (GRIS) and the He II maps (AIA) sample different temperatures, they may populate the same loops. We aligned the 64 GRIS He I line depression maps with the He II maps closest in time. The He I line depression maps are calculated by subtracting the average local continuum (which is constant) from the minimum value of the red component of each He I profile. This facilitates the comparison of loops in the two maps. Pearson's linear correlation coefficient was computed between matching He I and He II maps. Missing points in the He I maps caused by image rotation were excluded when computing the correlation coefficients. The mean correlation for the 64 maps is 72%. This is a significant correlation but also indicates that a one-to-one correspondence does not exist between the loops observed in He I and He II. Nevertheless, some loops seen in the neutral and ionized helium lines are likely the same loops but observed at different heights.

The time series of GRIS data covers about one hour. Averaging various quantities over this time interval reveals persistent chromospheric downflows (see movie attached to Fig. 3). In Sect. 4.2, we described a method to automatically identify dual-flow profiles in the He I triplet. Their presence is indicated by contours in Fig. 3. For each data set of the time series we created a binary mask containing the locations of dual-flow profiles. In every binary mask the pixels with dual flow profiles are

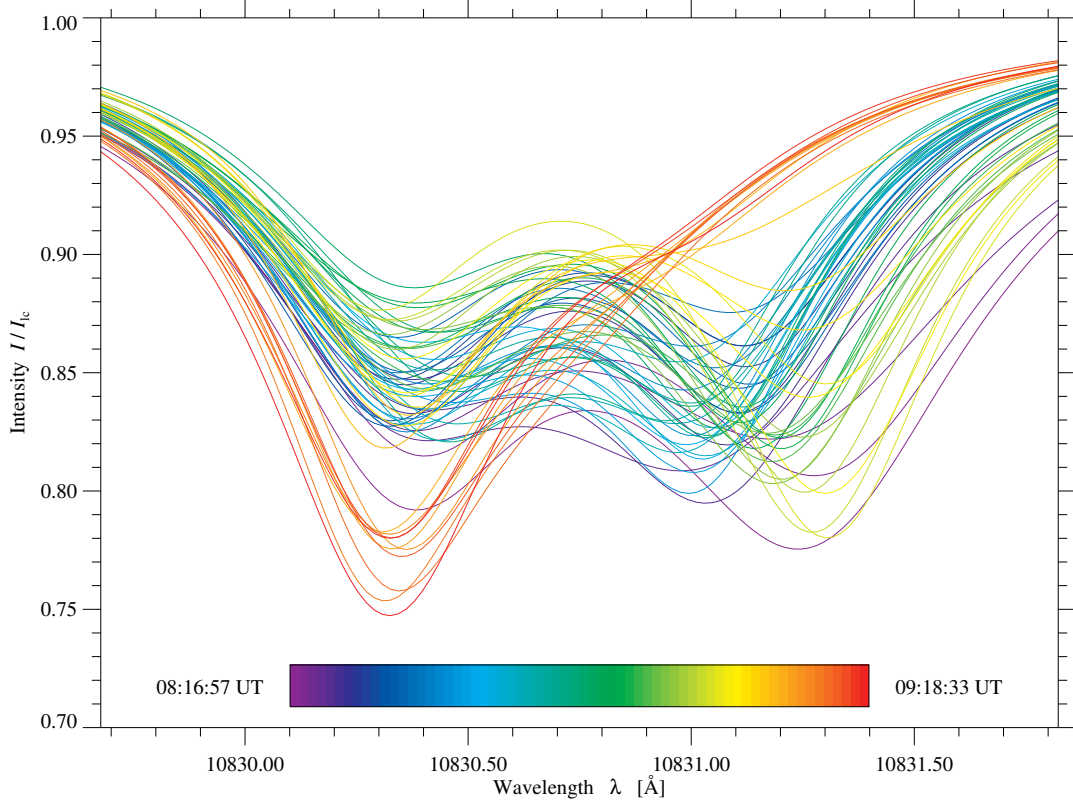


Fig. 6. Temporal evolution of the fitted spectral profiles (normalized to the local continuum intensity I_c) for the red component of the He I triplet. The rainbow-colored bar indicates the elapsed time after the start of the one-hour time series. The spectra were taken at a strong downflow kernel marked by a blue filled circle in the second panel of Fig. 3. These profiles are an average of all fitted spectral profiles within the blue patch and do not refer to individual fits. The spectra were slightly smoothed to avoid a cluttered display.

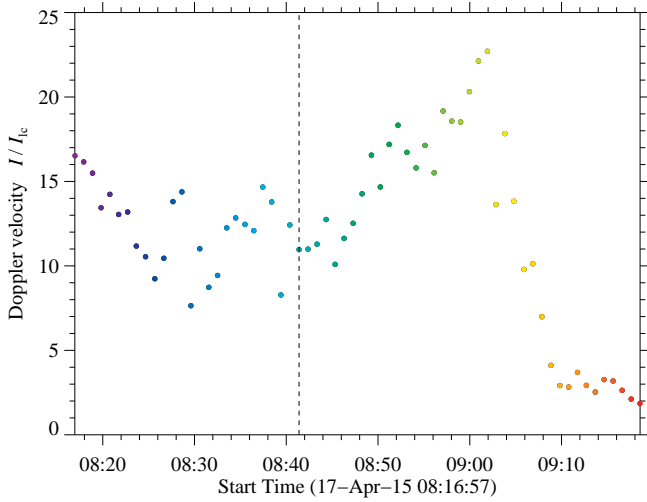


Fig. 7. Temporal evolution of the average Doppler velocities based on the He I triplet's red component in Fig. 6. The Doppler velocities were calculated either for a single flow component or refer to the fast component when dual flow components are present. The colors refer to the same profiles and times as in Fig. 6. The dashed vertical line marks the time when the profile shape starts to change rapidly with time in Fig. 6.

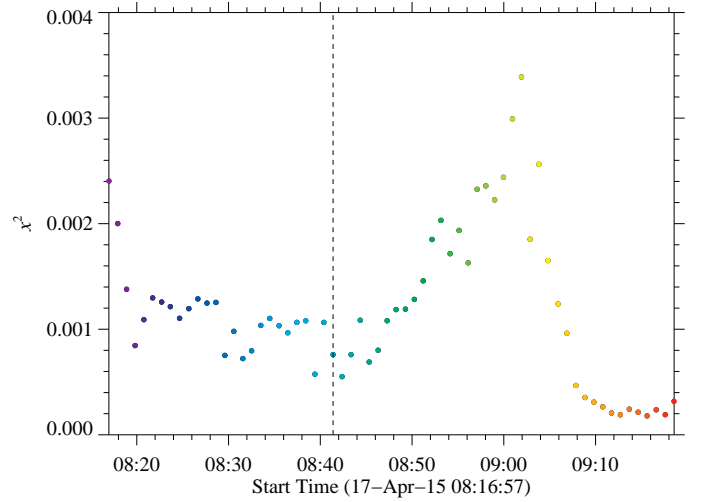


Fig. 8. Temporal evolution of the χ^2 -statistics for the single-Lorentzian fitting method.

marked by one and the rest with zero. Every map was added to obtain a final map with their frequency of occurrence shown in Fig. 5. Gray areas refer to regions where dual-flow profiles are absent, and red colors indicate that in more than 60 maps the

dual-flow profiles are present at the same location throughout the whole time series. Dual-flow profiles are mainly associated with the AFS, and are most common near the footpoints of arch filaments. However, at the location of pore P₁ they are almost absent during our observing time, while at the coordinates (44'', 10'') they are encountered more frequently for the negative polarity, and they are almost always present in the proximity of pore P₂, which exhibits the strongest downflows. One of the regions with

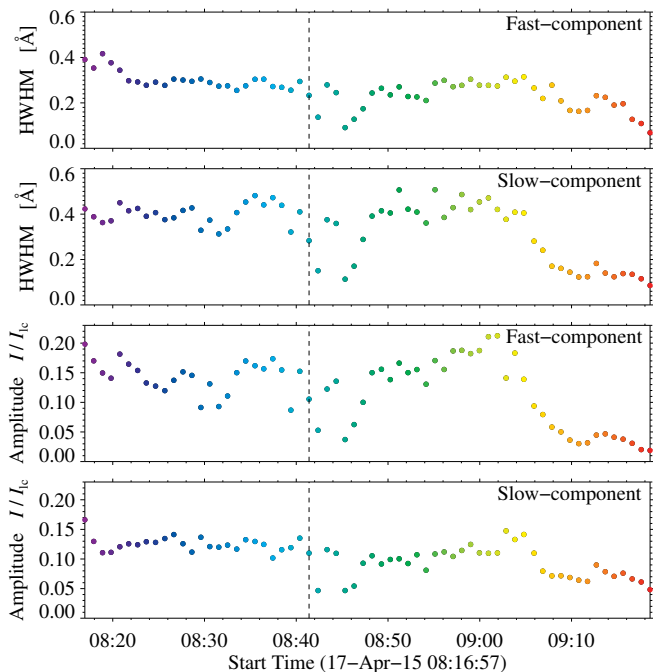


Fig. 9. Temporal evolution of the average HWHM of the He I (red) fast and slow component, and the average amplitude of the fast and slow component measured with the double-Lorentzian method. The number of dual-flow profiles contained within the blue circle in Fig. 3 varies with time between 18 and 69.

dual flow profiles in Fig. 5 is circular in shape ($63''$, $9''$), whereas the other is elongated and extends along a distinct and persistent arch filament with strong He I absorption ($58''$, $11''$).

5.3. Chromospheric dynamics near the leading pore

The temporal evolution of He I 10830 Å supersonic downflow intensity profiles near the leading pore P_2 was previously analyzed by González Manrique et al. (2017b), and are shown in their Fig. 4. The profiles correspond to an average of 69 spectra which are located inside the blue circle with a diameter of $1.4''$ shown in the line core intensity He I triplet map in Fig. 3. In total there are 64 such averaged profiles, one for each slit-reconstructed image. In the present study, we fitted these spectral profiles using the method described by González Manrique et al. (2016) and explained in Sect. 4.2. Accordingly, we fitted the 69 individual spectral profiles in every map, either with single- or dual-flow component Lorentzian fits, whichever is more appropriate. The number of dual-flow profiles within the blue circle varies between 18 and 69 during the time period from 08:16:57 UT to 09:18:33 UT. Thus, the average Doppler velocities contains both single- and double-peaked red components of the He I red profiles. In Fig. 6, we show the temporal evolution of the fitted spectral profiles. The inferred Doppler velocities are shown in Fig. 7, where every point in Fig. 7 corresponds to the average velocity of the 69 pixels within the blue circle in Fig. 3.

At the beginning of the time series, the slow and fast components had their minima well separated, forming a w-shaped profile with similar intensities in the line core (see Fig. 6). In the first 25 minutes of the times series the average values of the Doppler velocities fluctuated in the range of $7 - 17 \text{ km s}^{-1}$. The shape of the profiles changed very quickly with time. After 25 minutes, near 08:41 UT (marked as dashed line in Fig. 7), the minima of the two components are no longer well separated and

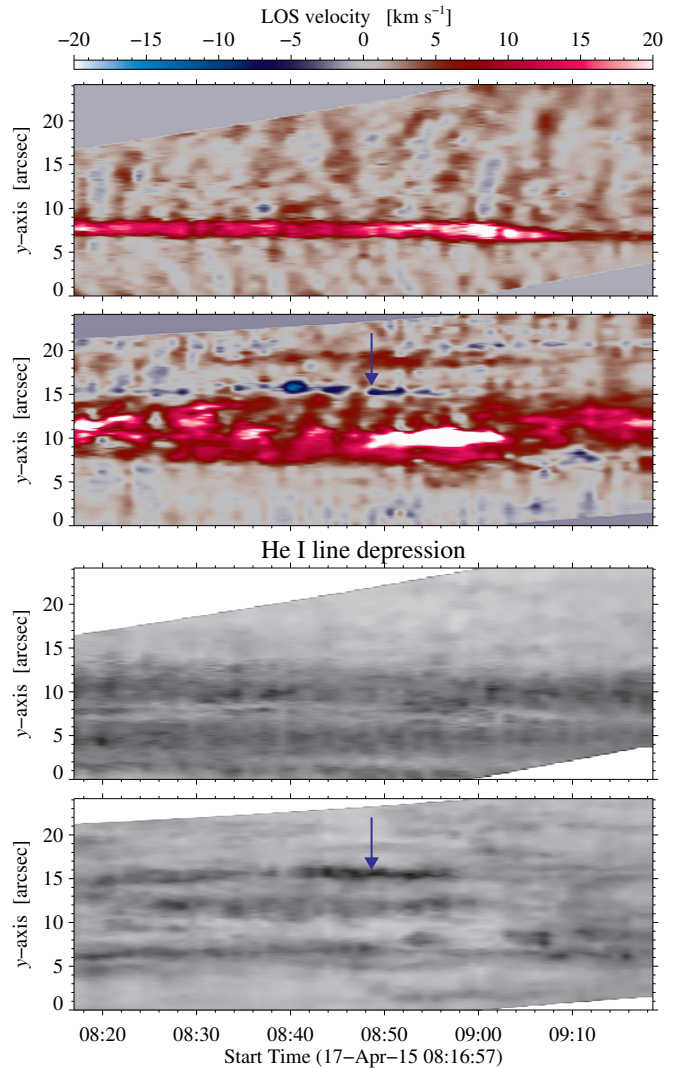


Fig. 10. Space-time diagrams of the He I Doppler velocity based on single-component fits (top two panels) and the He I line depression (bottom two panels). Both quantities are displayed for a footpoint (top and third panel) and a loop top (second and bottom panel) position of an arch filament. These positions are marked in Fig. 3 by vertical red lines. The reference rotation image is the same as presented in Fig. 3. The blue arrow points out the individual arch filament in Figs. 13 and 14. The Doppler velocities were calculated assuming single- or dual-flow components when present.

the intensity profile of the fast component becomes deeper. Starting around 08:41 UT the mean Doppler velocities also increased, reaching a maximum of about 23 km s^{-1} . The difference between line-core intensities of the two components reaches $\Delta I/I_0 \approx 0.1$. At the end of the time series, near 09:08 UT, the profiles change suddenly into single-component profiles with deeper line-core intensities than before. At this time, the majority of the profiles within the blue circle are single-component profiles. As a consequence, the Doppler velocities drop drastically to $2 - 4 \text{ km s}^{-1}$. This is consistent with the temporal evolution of the χ^2 -statistic for the single-Lorentzian fitting method (see Fig. 8) used to fit all 69 He I red component profiles within the blue circle in Fig. 3. The average χ^2 values are lower at the end of the time series, when more single-flow profiles are present.

The evolution of the half width at half minimum (HWHM) and the amplitude for the fast and slow components of the He I (red) component is measured with a double-Lorentzian (see

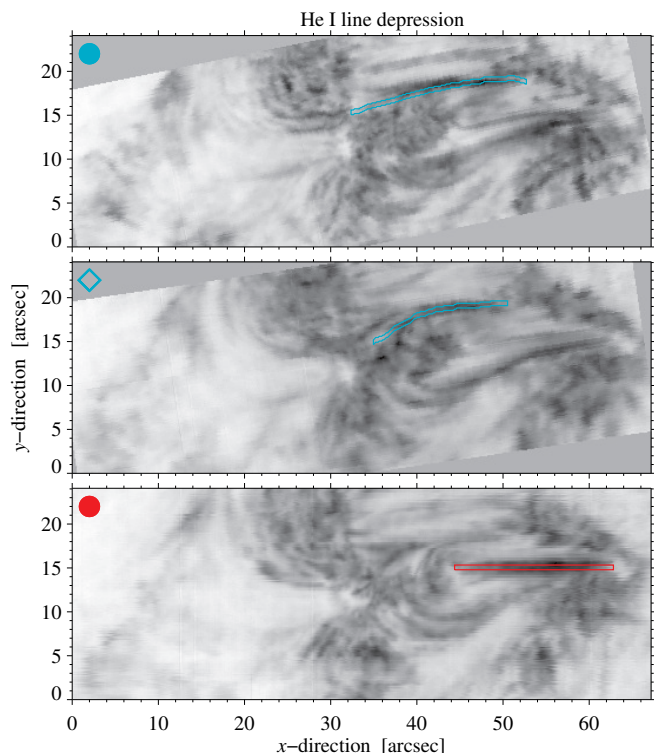


Fig. 11. He I line depression map at 08:16:57 UT (*bottom*), 08:40:23 UT (*middle*), and 08:49:16 UT (*top*) on 2015 April 17. The contours outline different arch filaments at different times. These images are rotated with respect to the reference image at 08:16:57 UT. The symbols and colors correspond to the arch filaments in Fig. 12.

González Manrique et al. 2016, Sect. 3, for more information). The HWHM for the slow and fast components exhibit a similar behavior. The width of the slow component usually exceeds the value of the fast component. Minimum values appear at the end of the time series and for a few minutes after 08:40 UT. At this time, the number of dual-flow profiles dropped to 18–22. An analogous behavior is observed for the amplitude of both the slow and fast components. The highest values correspond to profiles in Fig. 6 around 09:05 UT. The lowest parameters for the two components both match in time with the minimum values of the HWHM.

5.4. Tracking individual arch filaments

The second and bottom panels of Fig. 10 displays the temporal evolution close to the loop top of an arch filament, whereas the top and third panels show the temporal evolution of a footpoint close to the pore P₂. The positions are marked by the two red vertical lines in Fig. 3. The darkest region in the lower panel of Fig. 10 matches in time with the highest upflows in the second panel. An extended discussion of this figure is presented in Sect. 6.2.

We tracked in time the average Doppler velocities along an individual arch filament. Figure 11 contains three He I line depression maps at three different times. The contours depict three arch filaments at 08:16:57 UT (red contour/bullet), 08:40:23 UT (blue contour/square), and 08:49:16 UT (blue contour/bullet) on 2015 April 17. The two blue contours represent the same arch filament at different times. We inferred the Doppler velocities along the contours and calculated the mean values of five pixels in the y-direction for every position in the x-direction. The

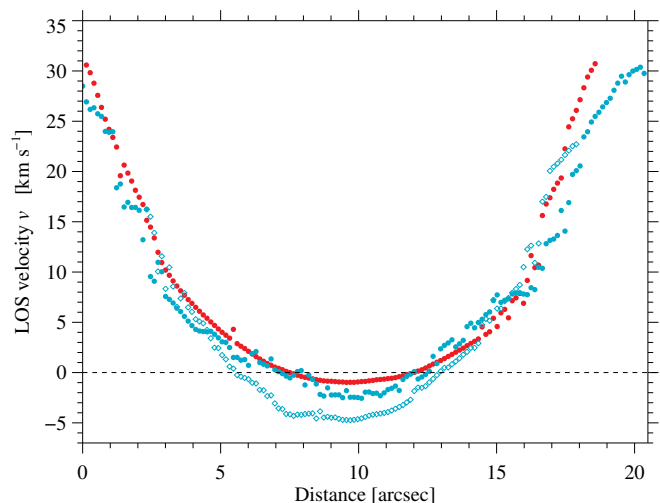


Fig. 12. Doppler velocities inferred from the He I triplet's red component. The Doppler velocities were calculated assuming single- or dual-flow components, whichever is more appropriate. The velocities are calculated along three arch filaments shown in Fig. 11. The colors of the contours and symbols (*upper left corners of panels in Fig. 11*) correspond to the contour lines in that figure.

mean LOS velocities for all three arch filaments are shown in Fig. 12. The loop tops show upflows (negative velocities) up to 6 km s⁻¹ and 2 km s⁻¹ in the case of the blue and red arch filaments, respectively. The distance between opposite-polarity footpoints are up to 20'' for the two arch filaments.

Next, we follow the temporal evolution of one individual arch filament and calculate the average Doppler velocities along it. We selected the arch filament outlined by a blue contour in Fig. 11. This arch filament is special since it emerged and disappeared during our observing sequence. Figure 13 shows the temporal evolution of the average Doppler velocities along the blue arch filament at six different moments. The lifetime of the arch filament is about 25–30 min, which is at the upper end of values (10–30 min) given in the literature (e.g., Chou 1993). Initially, the loop tops are nearly at rest, while there are small downflows near the footpoints. After approximately 10 min the loop tops exhibit the fastest average upflows (in the range of 5–6 km s⁻¹) and supersonic downflows with mean values of up to 31 km s⁻¹ are present at the footpoints. Near the end of the time series, the velocities approach zero in the whole arch filament. The upflows stop first, while the downflows still persist for another 20 min. In addition, the distance between the footpoints increases with time. At the beginning, the length of the arch filament was roughly 13'' while at the end of its lifetime the distance amounts to 21''.

We followed the temporal evolution of the average Doppler velocities at the loop tops and footpoints. The results are represented in Fig. 14 (*lower panel*). The black bullets represent the mean Doppler velocities at the loop top while the blue and red bullets indicate the mean Doppler velocities at the left and right footpoints, respectively. To calculate the average of the Doppler velocities at the loop tops, we selected the lowest negative value at the loop tops and the velocities in the two neighboring pixels on each side with a total of five values in Fig. 13. For the two footpoints, we selected five values, with the exception of the first and last pixels of the blue arch filament in Fig. 13. The individual arch filament appears in 33 out of 64 maps.

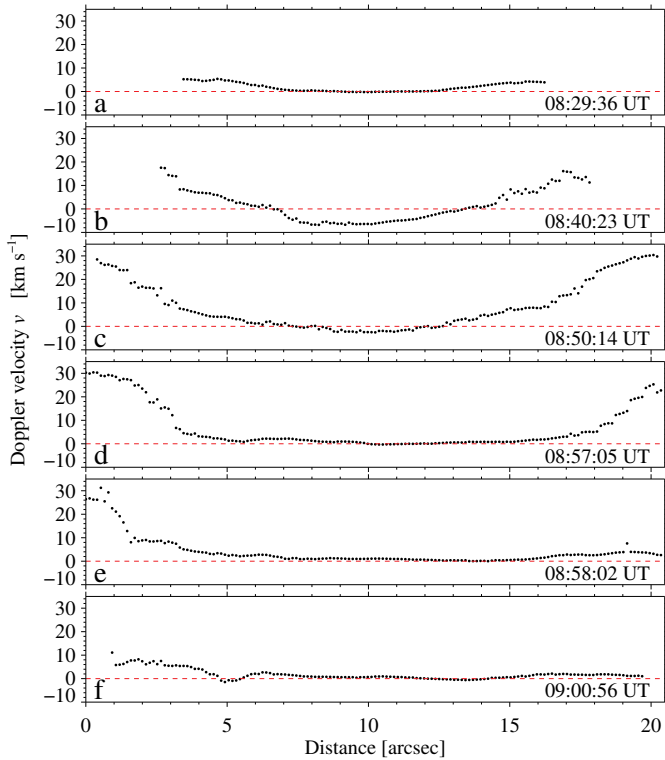


Fig. 13. Temporal evolution of the Doppler velocities along an individual arch filament (blue contours in Fig. 11) based on the He I triplet’s red component. The Doppler velocities were calculated based on either single- or dual-flow components.

In the middle panel of Fig. 14, we also followed the temporal evolution of the length of the individual arch filament during the same period. The evolution of the average He I line depression along the arch filament is also represented in the upper panel of Fig. 14. The values were normalized to one. A value of unity indicates the darkest part of the filament.

We found that the strongest upflows at the loop tops started at about 8:40 UT, and one minute later the downflows at the footpoints started to increase. Shortly before 08:40 UT the value of He I line depression was the lowest. After this time, the values increased. The length of the arch filament also increased at the same time. These downflows became very strong (more than 20 km s^{-1} on average) after two minutes in the case of the left footpoint (blue bullets in Fig. 14) and after around four minutes in the case of the right footpoint (red bullets in Fig. 14). The highest value of the He I line depression was also after four minutes. Afterwards the values slowly decreased. The downflows reached their highest velocity at the footpoints between 10–15 min after the upflow was detected at the loop tops. The arch filament was longest also about 15 min after the upflow was detected (08:55 UT). Afterwards, the downflows started to decay until the arch filament fully disappeared at 09:00 UT, i.e., 20 min after the downflows with the highest velocity were detected.

6. Discussion

6.1. Supersonic downflows near the leading pore

In the following, we investigate the temporal evolution of a chromospheric AFS connecting two photospheric pores. HMI magnetograms revealed both flux emergence and decay during the

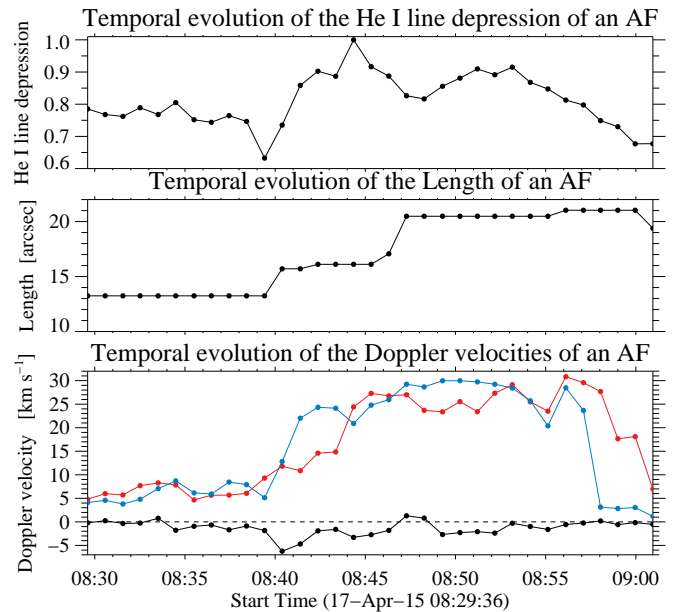


Fig. 14. Temporal evolution of the normalized mean He I line depression of the whole arch filament (*upper panel*). The highest value is the darkest. Temporal evolution of the length of the individual arch filament (*middle panel*). Temporal evolution of the mean Doppler velocities of the individual arch filament (*lower panel*) shown in Fig. 13. The Doppler velocities were calculated based on either single- or dual-flow components. The black bullets represent the mean Doppler velocities at the loop top and the blue and red bullets indicate the mean Doppler velocities at the left and right footpoints, respectively.

lifetime of the pores, which lasted about three days. We followed the dynamics of the AFS, where the Doppler velocity reached up to 40 km s^{-1} in single pixels. At the end of the observing period, the average values of the Doppler velocities dropped to $2\text{--}4 \text{ km s}^{-1}$. Several studies of AFS also based on the He I triplet reported supersonic downflows (e.g., Schmidt et al. 2000; Solanki et al. 2003; Aznar Cuadrado et al. 2005, 2007; Sasso et al. 2007; Lagg et al. 2007; Balthasar et al. 2016; González Manrique et al. 2016, 2017b).

Lagg et al. (2007) studied a similar case with supersonic downflows close to a growing pore. They reported on supersonic downflows at the footpoints of an emerging magnetic loop with LOS velocities of up to 40 km s^{-1} , as in our case. They observed during a time interval of about 70 min. Moreover, they studied a region near a pore with a small FOV ($3 \times 3 \text{ Mm}$) of one-minute and five-minute cadence for a total of 18 min with all the four Stokes parameters. In our case, scanning the ROI results in a one-minute cadence for the one-hour observing sequence, but without polarimetry. Lagg et al. (2007) observed persistent dual red components of the He I triplet. One slow component was always almost at rest while the fast component showed supersonic velocities within the same resolution element. We found exactly the same behavior near our growing leading pore (see Fig. 6).

Lagg et al. (2007) speculate that a flux tube is drained as a consequence of the pressure balance between the flux tube that is rising from the photosphere and the neighboring atmosphere. As a consequence, the hydrostatic support is lost and the material moves downwards to the solar surface. The theoretical draining time of the material for an individual arch filament is about 20 min (Chou 1993). This time is consistent with the estimations of Xu et al. (2010). Chou (1993) conjectured that the lifetime of an individual arch filament is between 10–30 min, but the entire

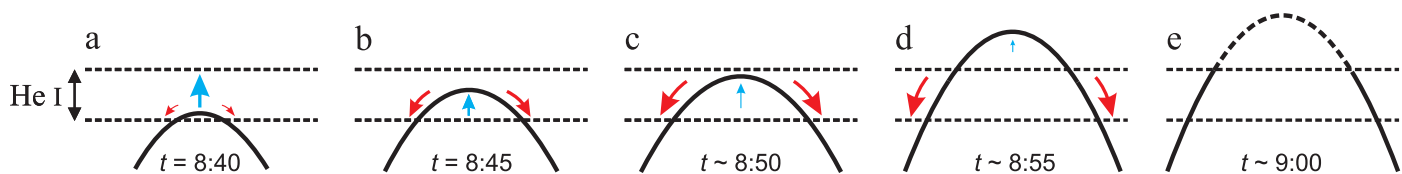


Fig. 15. Cartoon of the evolution of an individual arch filament (*from a to e*). Arrows in blue and red mark the direction of the plasma flows as observed in the He I triplet, respectively. The stronger the downflows (*red*), the thicker the arrow. The He I layer lies between the two dashed lines.

AFS will be visible as long as magnetic flux continues emerging. The lifetime of the arch filaments observed by us is in agreement with Chou (1993). In the present study, the observations agree with the findings of Lagg et al. (2007) that the upflows are located at the loop tops and the downflows are along the legs of the arch filaments.

Why are supersonic downflows seen near the pore? Typically, downflow speeds are larger when the atmosphere is cooler (as in the pore), since the final stratification will have less gas at chromospheric heights (due to the smaller pressure scale height). In addition, if the field strength is large (as in the pore), then the feature is strongly evacuated in the photosphere due to horizontal pressure balance. That means again that more gas has to be removed from the overlying arch filament, until hydrostatic equilibrium sets in.

6.2. Evolution of an individual arch filament

We agree with the assumptions of Chou (1993) and Lagg et al. (2007) who interpreted the strong downflows as a consequence of the draining of the rising loops that show up as arch filaments. To demonstrate that this is the most plausible hypothesis we studied the evolution of an individual arch filament (in another region of the FOV) that clearly emerges and decays during our GREGOR observing period.

One clear example of the emergence and decay of an individual arch filament is depicted with blue contours in Fig. 11. Its lifetime was about 30 minutes. During the emerging process the arch filament gradually gets darker, and while decaying it gets less dark and finally disappears. This behavior is clearly reproduced in the He I space-time diagram in Fig. 10 marked with a blue arrow. In particular, the second and fourth panels (from the top) follow the evolution of the loop tops. The individual arch filament appears at 15'' (y-axis). The arch filament becomes brighter with time because the material has drained, because it has moved out of the height range over which He I is formed, or because the gas has started getting hotter. Strong downflow LOS velocities appear at the same time as the arch filament became darker. The downflows disappear at the same time as the arch filament gets less dark and finally vanishes. The length of the arch filament changed during its lifetime.

We followed the evolution of the average Doppler velocities along the individual arch filament (Fig. 13) and focused on the loop top and the two footpoints (Fig. 14). Moreover, we also monitored the variations in the He I line depression and of the length of the arch filament. First, upflows of up to 6 km s^{-1} were detected at the loop tops. This value is comparable to the upflows found for example by Lagg et al. (2007) and Xu et al. (2010), but is smaller than the LOS velocity of 12 km s^{-1} found by Mein et al. (2000) from the IR Ca II 8542 Å. The Ca II spectral line is formed lower in the atmosphere than the He I triplet. Additionally, the high velocity values in Ca II can be attributed to AFSs behaving differently in different spectral lines. It is also possible that different observed AFSs behave differently.

Around 2–4 min later, strong downflows appeared at the footpoints which quickly increased to supersonic speeds, on average, up to 30 km s^{-1} . Simultaneously, the He I line depression is darkest. Similar results regarding the LOS velocities were presented by, e.g., Solanki et al. (2003), Lagg et al. (2007), and Xu et al. (2010). The upflows significantly decreased two minutes after they reached their maximum value. Conversely, the downflows reach their maximum values at the footpoints about 10–15 min later. The filament is longest about 15–20 min after the strong downflows appeared. The arch filament completely vanished 20 min after the strong upflows were measured (08:40 UT). The observations match the interpretation by Chou (1993) who conjectured that without upward transportation of material the loop could be emptied by drainage in around 20 min. Our observations also fit with the theoretical estimations made by Xu et al. (2010), who estimated that the loop is emptied by drainage in 20 min.

The observational evidence presented in this work leads to the scenario presented in the cartoon shown in Fig. 15. The cartoon represents the evolution of an arch filament (*from a to e*) similar to the individual filament studied here (in Figs. 13 and 14). This cartoon only represents the evolution seen in the He I.

In panel a, the individual arch filament is shown as it appears in He I line depression images ($t = 08:40 \text{ UT}$). The arch filament carries relatively cool plasma as it rises from the photosphere to the chromosphere. This panel represents the moment when the loop tops reach their maximum average LOS velocity (upward). In panel b the arch filament continues to rise, but with lower LOS velocities at the loop tops ($t = 08:45 \text{ UT}$). The cool material starts to drain toward the photosphere along the legs of the arch filament. The distance between the footpoints slightly increases. In panel c, the arch filament continues to rise with lower LOS velocities at the loop tops ($t = 08:50 \text{ UT}$). At the same time, the velocities at the legs increase and supersonic flows ($> 10 \text{ km s}^{-1}$) are already present close to the footpoints. The arch filament continues to expand horizontally. In panel d we speculate that the loop top has broken through the original He I formation height ($t = 08:50 \text{ UT}$), but He I is also present at the apex of the loop and down its sides (as found by Merenda et al. 2011). Formation of He I along the loop is due to the higher density in the loop than in its surroundings at this stage. As more material drains down the loop legs, the density in the loops continues to decrease. Hence, at some point the loop stops being dark in the He line core and we stop seeing major downflows along the legs. The last panel shows how the loop tops of the arch filament are disappearing from the He I observations. The material in the loop top is already in the higher layers of the atmosphere and the density must also have decreased there substantially. The average velocities of the loop tops are now very close to zero, as inferred from the He I triplet. The downflows at the footpoints and the upflows at the loop tops gradually decrease until the material within the flux tube is empty and the arch filament vanishes ($t = 09:00 \text{ UT}$). Typically, individual arch filaments are replaced by new arch filaments, which emerge

from below if enough flux is still available (Chou 1993). In line with Chou (1993) and Xu et al. (2010), our arch filament vanishes after 20 min counting from the strongest upflows seen in the loop tops (Figs. 10 and 14).

7. Summary and conclusions

We observed the temporal evolution of an arch filament system embedded in a bipolar emerging flux region with high cadence using the very fast spectroscopic mode of the GRIS instrument attached to the GREGOR telescope. One scan was carried out in about one minute and consisted of 180 slit positions with a step size of $0.135''$. The spectral region included the chromospheric He I 10830 Å triplet. We followed the AFS, which connected opposite polarities, during 64 minutes. The region did not carry enough flux to fully develop an active region.

During the observations, we detected several individual arch filaments. One filament was thoroughly tracked over its full lifetime of about 30 min, from the moment it appeared until it vanished. At the beginning, we inferred upflows in the loop top between 5 and 6 km s^{-1} . After 2–4 min, supersonic downflows started to appear with Doppler velocities in the range of $20\text{--}40 \text{ km s}^{-1}$. The arch filament expanded with time by about $7''$ in length during its lifetime (30 min). Our observations support predicted AFS scenarios by Chou (1993, and references therein) who hypothesized that the downflows in arch filaments could be explained by the emergence into the solar atmosphere of a flux tube. Lagg et al. (2007) suggested that the high-density gas carried by the rising loop drains down its legs due to the action of gravity and the simultaneous need for horizontal pressure balance and vertical hydrostatic equilibrium. As shown in the cartoon (Fig. 15), we follow the arch filament as it carries plasma during its rise from the photosphere to the corona. The material then drains toward the photosphere, reaching supersonic velocities, along the legs of the arch filament.

Near the leading pore (P_2), persistent chromospheric supersonic downflows were found for about 60 min. The peak value of these downflows reached 40 km s^{-1} . After one hour, the LOS velocities dropped from an average of 24 km s^{-1} to $1\text{--}7 \text{ km s}^{-1}$ in only seven minutes (Fig. 14). These findings support previous results of supersonic downflows inferred from the He I 10830 Å triplet in the vicinity of growing pores (Lagg et al. 2007).

In the present work, we mainly focused on the temporal evolution of an AFS as seen in the chromosphere using the He I 10830 Å triplet. In the next step we will investigate whether the plasma that drained along the legs of the arch filaments, exhibiting supersonic downflows near the footpoints, is detected in the photosphere.

Acknowledgements. The 1.5-meter GREGOR solar telescope was built by a German consortium under the leadership of the Kiepenheuer-Institut für Sonnenphysik in Freiburg with the Leibniz-Institut für Astrophysik Potsdam, the Institut für Astrophysik Göttingen, and the Max-Planck-Institut für Sonnensystemforschung in Göttingen as partners, and with contributions by the Instituto de Astrofísica de Canarias and the Astronomical Institute of the Academy of Sciences of the Czech Republic. SDO HMI data are provided by the Joint Science Operations Center – Science Data Processing. SJGM is grateful for financial support from the Leibniz Graduate School for Quantitative Spectroscopy in Astrophysics, a joint project of AIP and the Institute of Physics and Astronomy of the University of Potsdam; SJGM and PG acknowledge the support of the project VEGA 2/0004/16. CD has been supported by grant DE 787/3-1 of the German Science Foundation (DFG). MC acknowledges the support from the Spanish Ministry of Economy and Competitiveness through the project AYA2010-18029 (Solar Magnetism and Astrophysical Spectropolarimetry) for the development of the instrument GRIS. This project has received funding from the European Research Council (ERC) under the European Union’s Horizon 2020 research and innovation programme (grant agreement No. 695075) and has been supported

by the BK21 plus program through the National Research Foundation (NRF) funded by the Ministry of Education of Korea. This study is supported by the European Commission’s FP7 Capacities Program under the Grant Agreement number 312495. We would like to thank Drs. N. Bello González, C. Fischer, and R. Schlichenmaier for their help during the observing campaign.

References

- Archontis, V. 2012, *Phil. Trans. Roy. Soc. London Ser. A*, 370, 3088
- Avrett, E. H., Fontenla, J. M., & Loeser, R. 1994, in *IAU Symp.*, Vol. 154, *Infrared Solar Physics*, ed. D. M. Rabin, J. T. Jefferies, & C. Lindsey, 35
- Aznar Cuadrado, R., Solanki, S. K., & Lagg, A. 2005, in *ESA Spec. Publ.*, Vol. 596, *Chromospheric and Coronal Magnetic Fields*, ed. D. E. Innes, A. Lagg, & S. K. Solanki, 49.1
- Aznar Cuadrado, R., Solanki, S. K., & Lagg, A. 2007, in *Modern Solar Facilities – Advanced Solar Science*, ed. F. Kneer, K. G. Puschmann, & A. D. Wittmann, 173–176
- Balthasar, H., Gömöry, P., González Manrique, S. J., et al. 2016, *AN*, 337, 1050
- Berkefeld, T., Schmidt, D., Soltau, D., von der Lühe, O., & Heidecke, F. 2012, *AN*, 333, 863
- Brants, J. J. & Steenbeek, J. C. M. 1985, *Sol. Phys.*, 96, 229
- Bruzek, A. 1967, *Sol. Phys.*, 2, 451
- Bruzek, A. 1969, *Sol. Phys.*, 8, 29
- Buehler, D., Lagg, A., Solanki, S. K., & van Noort, M. 2015, *A&A*, 576, A27
- Caligari, P., Moreno-Insertis, F., & Schussler, M. 1995, *ApJ*, 441, 886
- Cheung, M. C. M. & Isobe, H. 2014, *Living Rev. in Sol. Phys.*, 11
- Cho, K. S., Bong, S. C., Chae, J., Kim, Y. H., & Park, Y. D. 2010, *ApJ*, 723, 440
- Chou, D. Y. 1993, in *ASP Conf. Ser.*, Vol. 46, *IAU Colloq. 141: The Magnetic and Velocity Fields of Solar Active Regions*, ed. H. Zirin, G. Ai, & H. Wang, 471–478
- Chou, D.-Y. & Zirin, H. 1988, *ApJ*, 333, 420
- Collados, M., López, R., Páez, E., et al. 2012, *AN*, 333, 872
- Denker, C., von der Lühe, O., Feller, A., et al. 2012, *AN*, 333, 810
- Druckmüller, M. 2013, *ApJSS*, 207, 25
- González Manrique, S. J., Bello González, N., & Denker, C. 2017a, *A&A*, 600, A38
- González Manrique, S. J., Denker, C., Kuckein, C., et al. 2017b, in *IAU Symposium*, Vol. 327, *IAU Symposium*, ed. S. Vargas Domínguez, A. G. Kosovichev, P. Antolin, & L. Harra, 28–33
- González Manrique, S. J., Kuckein, C., Pastor Yabar, A., et al. 2016, *AN*, 337, 1057
- Harvey, K. L. & Martin, S. F. 1973, *Sol. Phys.*, 32, 389
- Hirzberger, J. 2003, *A&A*, 405, 331
- Keil, S. L., Balasubramaniam, K. S., Smaldone, L. A., & Reger, B. 1999, *ApJ*, 510, 422
- Kuckein, C., Martínez Pillet, V., & Centeno, R. 2012, *A&A*, 542, A112
- Lagg, A., Woch, J., Krupp, N., & Solanki, S. K. 2004, *A&A*, 414, 1109
- Lagg, A., Woch, J., Solanki, S. K., & Krupp, N. 2007, *A&A*, 462, 1147
- Leka, K. D. & Skumanich, A. 1998, *ApJ*, 507, 454
- Lemen, J. R., Title, A. M., Akin, D. J., et al. 2012, *Sol. Phys.*, 275, 17
- Lites, B. W., Skumanich, A., & Martínez Pillet, V. 1998, *A&A*, 333, 1053
- Ma, L., Zhou, W., Zhou, G., & Zhang, J. 2015, *A&A*, 583, A110
- Markwardt, C. B. 2009, in *ASP Conf. Ser.*, Vol. 411, *Astronomical Data Analysis Software and Systems XVIII*, ed. D. A. Bohlender, D. Durand, & P. Dowler, 251–254
- Mein, P., Briand, C., Heinzel, P., & Mein, N. 2000, *A&A*, 355, 1146
- Merenda, L., Lagg, A., & Solanki, S. K. 2011, *A&A*, 532, A63
- Muglach, K., Schmidt, W., & Knölker, M. 1997, *Sol. Phys.*, 172, 103
- Muglach, K. & Sütterlin, P. 1998, in *ASP Conf. Ser.*, Vol. 155, *Three-Dimensional Structure of Solar Active Regions*, ed. C. E. Alissandrakis & B. Schmieder, 341
- Pariat, E., Aulanier, G., Schmieder, B., et al. 2004, *ApJ*, 614, 1099
- Parker, E. N. 1955, *ApJ*, 121, 491
- Penn, M. J. & Kuhn, J. R. 1995, *ApJL*, 441, L51
- Pesnell, W. D., Thompson, B. J., & Chamberlin, P. C. 2012, *Sol. Phys.*, 275, 3
- Quintero Noda, C., Shimizu, T., de la Cruz Rodríguez, J., et al. 2016, *Mon. Not. R. Astron. Soc.*, 459, 3363
- Sánchez Cuberes, M., Vázquez, M., Bonet, J. A., & Sobotka, M. 2003, *A&A*, 397, 1075
- Sankarasubramanian, K. & Rimmele, T. 2003, *ApJ*, 598, 689
- Sasso, C., Lagg, A., Solanki, S. K., Aznar Cuadrado, R., & Collados, M. 2007, in *ASP Conf. Ser.*, Vol. 368, *The Physics of Chromospheric Plasmas*, ed. P. Heinzel, I. Dorotović, & R. J. Rutten, 467
- Scherrer, P. H., Schou, J., Bush, R. I., et al. 2012, *Sol. Phys.*, 275, 207
- Schmidt, W., Muglach, K., & Knölker, M. 2000, *ApJ*, 544, 567
- Schmidt, W., von der Lühe, O., Volkmer, R., et al. 2012, *AN*, 333, 796
- Schmieder, B., Archontis, V., & Pariat, E. 2014, *SSR*, 186, 227
- Schou, J., Scherrer, P. H., Bush, R. I., et al. 2012, *Sol. Phys.*, 275, 229

- Sobotka, M., Del Moro, D., Jurčák, J., & Berrilli, F. 2012, *A&A*, 537, A85
- Solanki, S. K., Lagg, A., Woch, J., Krupp, N., & Collados, M. 2003, *Nature*, 425, 692
- Spadaro, D., Billotta, S., Contarino, L., Romano, P., & Zuccarello, F. 2004, *A&A*, 425, 309
- Strous, L. H., Scharmer, G., Tarbell, T. D., Title, A. M., & Zwaan, C. 1996, *A&A*, 306, 947
- Tsiropoula, G., Georgakilas, A. A., Alissandrakis, C. E., & Mein, P. 1992, *A&A*, 262, 587
- van Driel-Gesztelyi, L. & Green, L. M. 2015, *Living Reviews in Solar Physics*, 12, 1
- Vargas Domínguez, S., van Driel-Gesztelyi, L., & Bellot Rubio, L. R. 2012, *Sol. Phys.*, 278, 99
- Verma, M. & Denker, C. 2014, *A&A*, 563, A112
- Volkmer, R., Eisenträger, P., Emde, P., et al. 2012, *AN*, 333, 816
- Xu, Z., Lagg, A., & Solanki, S. K. 2010, *A&A*, 520, A77
- Zwaan, C. 1978, *Sol. Phys.*, 60, 213
- Zwaan, C. 1985, *Sol. Phys.*, 100, 397
- Zwaan, C. 1987, *ARA&A*, 25, 83